

Accurate Efficiency Measurements of Organic Light-Emitting Diodes via Angle-Resolved Spectroscopy

Emily Archer, Sabina Hillebrandt, Changmin Keum, Caroline Murawski, Jan Murawski, Francisco Tenopala-Carmona, and Malte C. Gather*

The accurate characterization of thin-film light emitting diodes (LEDs)—including organic light emitting diodes (OLEDs), perovskite LEDs, and quantum dot LEDs—is crucial to the understanding of the factors that influence their efficiency and thus to the fabrication of LEDs with improved performance and stability. In addition, detailed information about the angular characteristics of LED emission is useful to assess the suitability of individual architectures, e.g., for display applications. Here, the implementation of a goniometer-based measurement system and corresponding protocol are described that allow to accurately determine the current–voltage–luminance characteristics, external quantum efficiency, and luminous efficacy of OLEDs and other emerging thin-film LEDs. The system allows recording of angle-resolved electroluminescence spectra and accurate efficiency measurements for devices with both Lambertian and non-Lambertian emission characteristics. A detailed description of the setup and a protocol for assembling and aligning the required hardware are provided. Drawings of all custom parts and the open-source Python software required to perform the measurement and to analyze the data are included.

color-tunable emission, they are particularly attractive for applications in self-emissive flat-panel displays.^[2,3] Due to the compatibility of OLED technology with low-cost production approaches, such as solution-based printing methods, OLEDs are also considered for large-area, thin, lightweight, and glare-free ambient illumination.^[4–7] In the future, commercial devices may also exploit the fact that OLEDs are compatible with a range of different substrates, including mechanically flexible ones.^[8–10] There has also been interest in adapting OLED technology for applications beyond the display and lighting sector, e.g., for biomedical use or optical communications.^[11–16] Meanwhile, a number of other material platforms, e.g., perovskites and quantum dots, quickly gain prominence for thin-film LED light-sources, and each of these have specific benefits and challenges when compared to OLED technology.^[17–20]

1. Introduction

Organic light-emitting diodes (OLEDs) have gained much attention from both research and industry in the over 30 years since the first device was reported.^[1] As solid-state light sources with

In order to compare different materials and device architectures, reliable and accurate measurements of device efficiency are crucial. Yet, there are a number of difficulties associated with this, which mainly arise from the extended emissive area of OLEDs and other thin-film LEDs, from the use of transparent and often light-guiding substrates, and from the fact that the angular emission characteristics can vary drastically between devices. Despite decades of research into OLEDs, the community still uses a number of different measurement techniques and there is no universal standard.^[21] Up to this date, a significant number of publications report efficiency estimates from oversimplified measurements and a substantial fraction of these appear to overestimate the real device efficiency.


Here, we describe the implementation of a goniometer-based measurement setup that can record the electroluminescence spectrum of an OLED or other LED with extended emissive area under different angles to accurately determine their emission characteristics and efficiency. We explain in detail the design, assembly, and alignment of the goniometer and the procedure used to extract the device efficiency from the measured data. We provide examples that illustrate how the angle-resolved measurement leads to a significantly more accurate efficiency value, compared to, e.g., just recording the intensity emitted in the forward direction. Our motivation for using an angle-resolved method over other approaches, in particular over a measurement based on an integrating sphere, is that it is more flexible and less prone to calibration artefacts. In addition, the

E. Archer, Dr. S. Hillebrandt, Dr. C. Keum, Dr. C. Murawski, Dr. J. Murawski, Dr. F. Tenopala-Carmona, Prof. M. C. Gather
Organic Semiconductor Centre
SUPA

School of Physics and Astronomy
University of St Andrews
North Haugh KY16 9SS, UK
E-mail: mcg6@st-andrews.ac.uk

Dr. C. Murawski
Kurt-Schwabe-Institut für Mess- und Sensortechnik Meinsberg e.V.
Kurt-Schwabe-Str. 4, 04736 Waldheim, Germany

Prof. M. C. Gather
Centre for Nanobiophotonics
Department of Chemistry
University of Cologne
Greinstr. 4–6, 50939 Köln, Germany

 The ORCID identification number(s) for the author(s) of this article can be found under <https://doi.org/10.1002/adom.202000838>.

© 2020 The Authors. Advanced Optical Materials published by Wiley-VCH GmbH. This is an open access article under the terms of the Creative Commons Attribution License, which permits use, distribution and reproduction in any medium, provided the original work is properly cited.

DOI: 10.1002/adom.202000838

angular emission characteristics of OLEDs are often of importance in their own right, e.g., to assess the suitability of a certain device architecture for use in a display or in general illumination. We also describe a simple modification of our setup that allows an estimate of the internal device efficiency. Finally, we discuss modifications to record angle-resolved thin-film photoluminescence, which can be used to determine emitter dipole orientation.^[22–24] Our description is sufficiently detailed to readily allow replication of our system in a different lab. The system is built almost exclusively from standard components, with a detailed list provided. For optimal usability a few customized parts are required, and these can be produced from the drawings provided, e.g., in a mechanical workshop or through use of 3D printing. The software to operate the setup and to perform the required data analysis is made available as open source through a repository and on GitHub for extension and modification by others.

This paper is structured as follows: Section 2 provides a general introduction to OLED efficiency and the approaches described in the literature; Section 3 discusses the goniometer setup, including parts, assembly, alignment, calibration, and measurement procedures; Section 4 describes the theory used to determine angle correction factors and thus the relevant measures of device efficiency for OLEDs with Lambertian and non-Lambertian emission characteristics; Section 5 shows examples of measurements for different OLEDs; and Section 6 discusses modifications and further applications of the system, including estimating internal device efficiency, recording angle-resolved photoluminescence of thin films for characterization of molecular orientation, and automated measurements on multiple OLEDs on one substrate. A detailed parts list, all additional derivations, and a link to the drawings of customized parts and the open source software to operate the system can be found in the Supporting Information.

2. Background

An OLED typically consists of a stack of organic layers between an anode and a cathode, at least one of which is partially transparent, as shown in **Figure 1**. Charges are injected into the electron transport layer (ETL) and hole transport layer when a voltage is applied across the device. The charges then migrate through the hole blocking layer and electron blocking layer into the emissive layer (EML) in the center of the device. In the EML, the charges recombine to form excitons, which then decay radiatively, i.e., under emission of a photon.

OLED efficiency is often expressed in terms of the external quantum efficiency (EQE), which is the proportion of charge carriers injected into the device that are converted to photons and then ultimately leave the device as useful emission,

$$\eta_{\text{EQE}} = \gamma \eta_{\text{S/T}} \eta_{\text{eff}} \eta_{\text{out}} \quad (1)$$

The EQE depends on a combination of several factors; namely the balance of charge carriers γ , the spin factor $\eta_{\text{S/T}}$ (which describes the fraction of singlet or triplet excitons that can decay radiatively in electroluminescence), and the effective radiative efficiency η_{eff} . Combined, these factors constitute

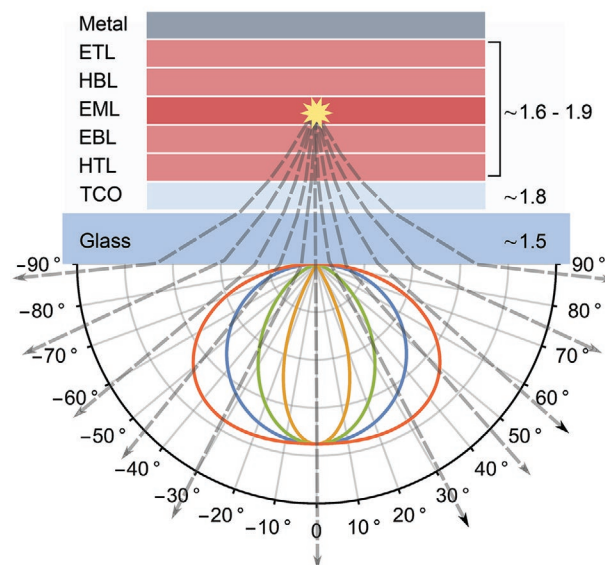


Figure 1. Schematic illustration of a bottom-emitting OLED consisting of a series of organic layers sandwiched between a transparent conductive oxide (TCO) and a metal electrode. Light generated in the emissive layer (EML) is refracted at the different interfaces within the OLED before leaving the structure (dashed grey lines). Approximate refractive indices of the different layers in the visible range (n) are indicated on the right-hand side of the stack. The lower part of the sketch illustrates different angular characteristics of emission. Blue, ideal Lambertian; green, slightly sub-Lambertian; orange, highly sub-Lambertian; and red, super-Lambertian.

η_{IQE} , the internal quantum efficiency (IQE). The fraction of the internally generated photons that ultimately leaves the device is quantified by the outcoupling efficiency, η_{out} . Through optimizing the balance of electron and hole injection and developing highly efficient emitters that harvest triplet excitons through phosphorescence or thermally activated delayed fluorescence, OLEDs with IQEs approaching 100% have been realized.^[25,26]

Despite this, the EQE of most OLEDs is limited to around 30% or less, as the majority of photons remain trapped in the OLED, even in state-of-the-art devices.^[27] These losses are caused by mismatches in the refractive indices n leading to trapped modes due to total internal reflection, coupling to surface plasmon modes, substrate modes, and absorption within the device.^[28] The low outcoupling efficiency of most OLEDs has led to the development of strategies to enhance light extraction, such as internal outcoupling structures, external outcoupling structures, and horizontally orientated emitters.^[29–35] The EQE is linked to the number of photons generated by an OLED. However, for many applications the brightness of OLEDs as perceived by a human observer is more important. This is quantified by photometric quantities, like the luminous efficacy.

A common method to estimate the EQE is to perform a scan of different voltages applied to the OLED while detecting current density and light output in forward direction. This can be realized with a luminance meter or by measuring the signal from a photodiode facing the OLED from a distance that is much larger than the size of the OLED and the photodiode. After also measuring the electroluminescence spectrum, the radiant

intensity and the luminance of the OLED in the forward direction, i.e., perpendicular to its surface, can then be calculated. Due to the self-emissive nature of OLEDs, it is often assumed that the angular distribution of their emission follows the ideal Lambertian profile, i.e., that the radiant intensity has a cosine dependency on the viewing angle θ , so $I(\theta) = I_0 \cos \theta$. If the Lambertian assumption is justified, the total emitted radiant flux can be calculated by simply integrating $\cos \theta$ over all solid angles. However, in many cases, the Lambertian assumption leads to an over- or underestimation of the device efficiency as the angular emission characteristics of OLEDs can deviate substantially from the ideal Lambertian as illustrated in Figure 1.

One way to circumvent this problem is the use of an integrating sphere, a hollow cavity that is internally coated with a diffusely reflecting material. Placing an OLED inside an integrating sphere leads to integration of the light over all angles and, thus, enables measuring in a single measurement the total radiant flux emitted by the device.^[36] This measurement requires delicate calibration of the system and any change in the absorption or reflectivity of the OLED means that the calibration needs to be updated. In addition, an integrating sphere measurement provides no information about the angular dependence of the OLED emission spectrum or emission intensity. However, knowledge and optimization of the angular emission characteristics of OLEDs are very important for many applications, in particular for their use in displays.

An alternative to an integrating sphere is to record the relative emission intensity and the electroluminescence spectrum of the OLED at each angle, e.g., by using a goniometer. This information can then be employed to determine a correction factor that converts a calibrated measurement of the amount of light the OLED emits in forward direction into the total amount of light emitted by the device. Thus, all relevant performance characteristics of the OLED, including EQE and luminous efficacy, can be calculated. Measuring intensity and spectrum at each angle is much less prone to changes in the absorption or reflectivity of the OLED but more time-consuming compared

to using integrating spheres. In addition to yielding device efficiency, the goniometer measurement provides useful further data and is more robust to changes of sample characteristics and thus often more precise.^[37] However, as will be discussed in Section 3, the goniometer approach requires careful design and thorough initial alignment to obtain angular emission characteristics with sufficient accuracy to deduce correct efficiency values.

For both the integrating sphere and the goniometer-based measurement, it is important to exclude light emitted at the edge of the OLED substrate. Edge emission originates from light that is trapped and guided within the substrate. Due to absorption in the substrate, the amount of edge emission depends strongly on substrate size and geometry, with larger substrates showing a lower fraction of edge emission relative to the forward emission (the light is generated further away from the edge and thus more strongly absorbed). For OLED-based lighting, devices are typically much larger than the test pixels used for device optimization. In OLED displays, edge emission does not contribute to the display brightness and needs to be blocked.

3. Measurement

3.1. Overview

Measuring the spectrum and intensity of the light emitted by an OLED at different angles with respect to its surface orientation can generally be achieved in two ways; either by moving the detector around a fixed OLED, or by rotating the OLED about a central axis of rotation relative to a fixed detector. Our method follows the latter approach as this is in practice simpler to set up and align and is more conducive to a compact system. The system is aligned along two principal perpendicular axes as shown in Figure 2. The OLED sample is positioned on top of a motorized rotation stage and its axis of

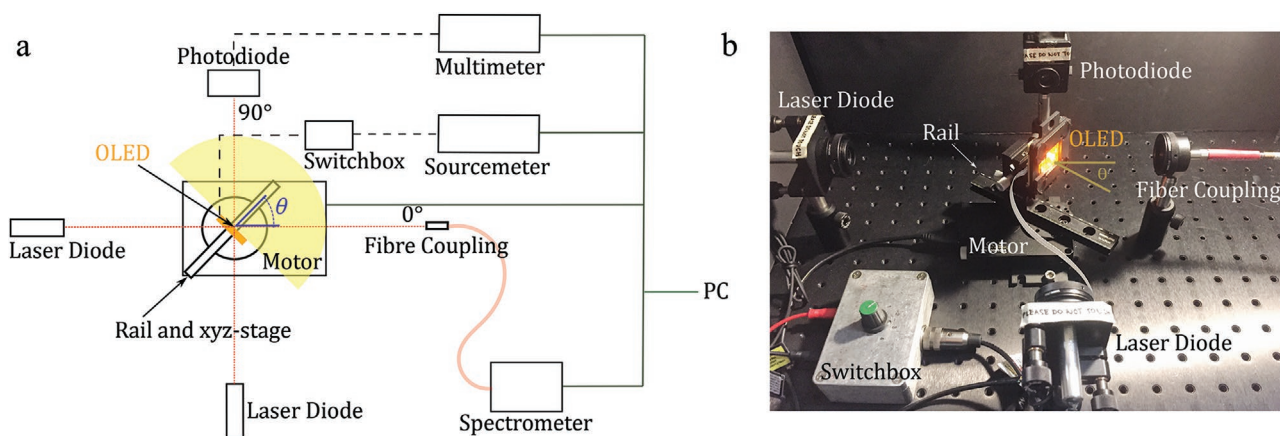


Figure 2. a) Diagram of the goniometer-based measurement system for recording angle-resolved OLED emission. The OLED (orange rectangle) is mounted on a motorized rotation stage using a rail and an xyz-stage. The emission cone of the OLED is indicated by a yellow half circle. Two red laser diodes mark the principal axes of the system (dotted red lines), their crossing point is set to the axis of rotation. The OLED is driven by a PC controlled sourcemeter through a switchbox to select the active pixel on the device. A fiber-coupled spectrometer and a photodiode connected to a multimeter detect the OLED emission as a function of the angle θ . b) Photograph of the actual setup with one pixel on the OLED substrate in operation. The multimeter, sourcemeter, spectrometer and PC are not shown.

rotation is aligned to the intersection of the two perpendicular axes with the help of two laser diodes that act as their physical representation. We use two separate detectors, a photodiode and a fiber spectrometer. The photodiode and the end facet of the fiber that is coupled to the spectrometer are mounted at mutually perpendicular positions along each principal axis. The distance between the OLED and the photodiode and the collection fiber each must be much larger (e.g., >20-fold) than the dimension of the OLED, the diameter of the photodiode's active area and of the collection fiber. This is required so that the solid angle of the OLED emission that is subtended by the photodiode and the collection fiber can each be approximated to be infinitesimally small. In our setup, the separation between OLED and photodiode as well as between OLED and collection fiber was 115 mm.

For the measurement, the OLED is first rotated to face the photodiode. The photodiode voltage and OLED current are measured while scanning the voltage applied to the OLED across the range of interest. Next, the angle-dependent electroluminescence of the device is measured. For this, the OLED is rotated through 90° or 180° in angular increments, usually of 1°, and at each increment a spectrum of the device is taken by the spectrometer. From this data, the current–voltage–luminance (IVL) characteristics of the device, the EQE, and the power efficacy are then computed. The measurement and calculation of all quantities is fully automated and controlled by a custom software written in Python (see Section 3, Supporting Information).

3.2. Parts and Assembly of the Electroluminescence Goniometer

A detailed list of the parts required to assemble the setup is provided in Sections 1.1 and 1.2 (Supporting Information). The entire setup is mounted on an optical breadboard and enclosed by black cardboard to prevent stray light from entering the system and to minimize the risk of exposure to the alignment lasers. The setup is centered around the rotation stage which carries an optical rail with an xyz-stage and a sample holder that provides electrical contact to the OLED pixels. The rail is used for coarse alignment of the device to the axis of rotation, the xyz-stage allows fine alignment, and positioning of the sample holder to the OLED pixel of interest. The two diode lasers used for alignment are positioned using optical posts. Their tilt in the horizontal and vertical direction is adjusted via kinematic mounts. The spot size of the laser beam can be adjusted for fine calibration with iris apertures mounted in front of each laser. The photodiode is positioned at the back of the enclosure, again mounted via a standard optical post, and faces toward the sample and the front laser diode. The photodiode used has an integrated transimpedance amplifier and thus its own power supply and is connected to a multimeter via a coaxial cable. The spectrometer fiber is mounted on a standard optical post assembly with a fiber adapter and is positioned on the right-hand side of the enclosure. The fiber is oriented such that it faces the OLED and the alignment laser on the left-hand side of the enclosure. The other end of the fiber is connected to a spectrometer. The

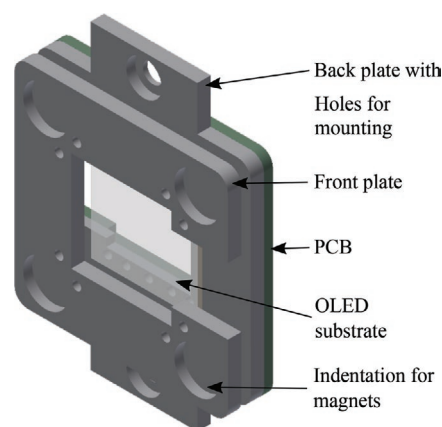


Figure 3. 3D rendering of customized sample holder for top- and bottom-emitting OLEDs fabricated on 24 × 24 mm² substrate. The holder consists of two parts, held together with magnets. The back part of the holder contains a printed circuit board (PCB) with contact pins and cable connector to make electrical contact to the OLED pixels.

OLED is driven by a sourcemeter via a switchbox that connects to the sample holder. The multimeter, sourcemeter, rotation stage, and spectrometer are all connected to a PC via USB connections.

The switchbox and the sample holder were both fabricated in-house. **Figure 3** shows a 3D rendering of the sample holder used; detailed drawings are provided for download (Section 1.1, Supporting Information). The holder is designed for substrates measuring 24 × 24 mm² and is compatible with both bottom- and top-emitting OLEDs. It is formed by a front and a back plate which sandwich the OLED in between and which are held together by magnets located in all four corners. A printed circuit board (PCB) with gold-coated contact pins is attached to the backside of the back plate to make electrical contact to the anode and cathode contact pads on the OLED substrate. The sample holder is mounted on the xyz-stage with holes provided in the back plate. The front and back plate have a cut-out on one side to allow for emission to be detected in top- and bottom-emitting OLEDs at angles up to nearly 90°. In order to prevent the detection of light that is guided in the substrate and emitted at the edges and thus not contributing to the useful emission of the measured pixel, the exposed substrate edge in the region of the cut-out needs to be shielded, e.g., by black tape (The other three substrate edges are masked by the sample holder itself).

The configuration of sample holder and switchbox used here was chosen to allow addressing and measuring of all pixels on an OLED substrate in a simple manner. The need for a custom-made switchbox can be eliminated and the design of the sample holder can be considerably simplified by connecting the OLED directly to the sourcemeter, e.g., via alligator clips, provided the connection is secure during rotation.

3.3. System Alignment

Once all components are positioned on the optical breadboard, it is important to ensure that they are accurately aligned with respect to the two perpendicular axes of the system and that these two principal axes intersect exactly on the axis of rotation

(which is located at the center of the mounting plate of the rotation stage). Deviation of any component from these axes distorts or skews the measured angular emission characteristics and will thus lead to inaccurate efficiency measurements. In particular, the active pixel of the OLED to be measured must always be positioned at the center of the axis of rotation to avoid any lateral movement during rotation. This is ensured by positioning the OLED such that the two laser beams representing the two perpendicular axes of the system overlap at the center of the OLED pixel.

The general principle for alignment is to initially align both lasers to the axis of rotation. For this, we first ensure that the spectrometer fiber and the photodiode are shielded from the laser emission so that there can be no damage to either from the alignment lasers. With an OLED sample mounted on the rotation stage, it is useful to first coarsely adjust the lasers to the height of the sample. All components on the rotation stage, down to the alignment rail, are then removed to leave just the bare mounting plate. The vertical tilt of the lasers is then adjusted so that their beams are parallel to the optical breadboard; this can be checked by measuring the height of the laser beam close to and further away from the laser, and repeatedly adjusting the vertical tilt until the spot height is consistent over the entire length of the optical breadboard. It is important to ensure that the height of both lasers is the same. An optical post is then screwed into the center of the mounting plate on the rotation stage to mark the axis of rotation. The horizontal tilt of the lasers is adjusted until both lasers shine directly onto the center of this post, thereby ensuring that the intersection of the laser beams now marks the center of rotation. After removing the post, the height of the photodiode and spectrometer fiber adapter are adjusted until the laser spot is over the center of each. For this step, it is important to switch off the photodiode amplifier and the spectrometer to avoid damage. It is furthermore important to ensure that the photodiode and the spectrometer fiber are both oriented exactly perpendicular to the principal axes of the system. This is done by adjusting their tilt until the light reflected back from each overlaps with the emission aperture of the corresponding laser.

3.4. Sample Alignment

Once the system is aligned, the alignment rail is placed back onto the mounting plate of the rotation stage. It may be useful to note the angle at which the rail sits with respect to the angle graduation on the rotation stage so that the rail can be repositioned at roughly the same angle if it needs to be removed at a later stage. The *xyz*-stage is then slid onto the rail and the sample holder is fixed on the *xyz*-stage. A dummy substrate covered with opaque tape on one side is inserted into the sample holder. The tape should be on the same side of the substrate as the organic layers of the actual device to be measured. This ensures that after calibration the active OLED pixel is located exactly on the axis of rotation. Next, the position of the *xyz*-stage along the rail is adjusted until the two laser spots overlap on the surface of the tape attached to the dummy substrate. This overlap should occur consistently for a range of angles; if the spots appear to move as the stage is rotated, the

initial alignment procedure should be repeated. The dummy substrate is then replaced by an actual OLED and the rotation stage is homed to the 0° position.

Next, the angle position of the rotation stage for which the sample faces the spectrometer fiber must be found as it is generally not possible to position the rail accurately enough by hand. Using the software package provided in Section 3 of the Supporting Information, the motor can be moved to varying angles until the sample faces the spectrometer fiber and the angle setting corresponding to the 0° position is found. (We define $\theta = 0^\circ$ as the position where the sample faces the spectrometer fiber; $\theta = 90^\circ$ means the sample faces the photodiode.) For finer calibration of the true 0° position, it is then useful to rotate the OLED by -90° so that it faces one of the two calibration lasers and to then fine tune the angle of the rotation stage until the back-reflection from the laser overlaps with the emission aperture of that laser. Finally, with the OLED still facing one of the lasers, its position is adjusted with the *xyz*-stage until the laser spot is at the center of the OLED pixel that is to be measured. During this final step, care must be taken to not move the OLED backward or forward along the rail and along the laser beam, but to restrict any movement to the direction perpendicular to the rail. This is because movement along the rail moves the OLED away from the axis of rotation. If the OLED is accidentally moved away from the axis of rotation, the sample alignment should be repeated.

3.5. Measurement Procedure

Before starting the measurement, the sample is rotated to $\theta = 90^\circ$ so that it faces the photodiode. The data for the *IVL* characteristics is then recorded by measuring the OLED current and photodiode voltage for a range of voltages applied to the OLED. For this voltage scan we normally use coarser steps at lower voltages, i.e., below the OLED turn-on voltage, and finer steps at higher voltages. The sourcemeter applies the desired voltage to the designated OLED pixel via the switchbox and reads back the OLED current, while the multimeter simultaneously reads the voltage from the photodiode. The data are then saved in a text file.

Next, the software moves on to record emission spectra of the OLED at different angles of observation. First, a background spectrum is taken by the spectrometer with the OLED turned off. Next, the sample is rotated to each of the angles specified, i.e., typically going through a 0...90° or $-90...90^\circ$ sector in steps of 1°. Once the motor has reached each designated angle, the OLED is turned on and the spectrometer records a spectrum. The OLED is then turned off again and the motor moves to the next angle. During this measurement, the OLED is typically driven at a constant current (rather than at a fixed voltage) to minimize changes in OLED brightness due to temperature drift and possible device degradation during the measurement. For each angle position, our analysis software subtracts the background spectrum, and smoothens the spectrum, typically by applying a 10 nm sliding average filter. This filters out thermal and shot noise that inevitably occurs due to the requirement for a narrow collection angle and the resulting low light collection efficiency.

The spectra obtained in this way are in raw CCD counts and are therefore still skewed due to the wavelength dependent detection efficiency of the spectrometer and the wavelength dependent transmission of the fiber. To convert the spectra into a measure proportional to the spectral radiant intensity (which has units of $\text{W nm}^{-1} \text{sr}^{-1}$), the software multiplies them by a calibration spectrum of the system that contains the energy per count and per nm at each wavelength. We note that it is not necessary to obtain an absolute measurement of spectral radiant intensity as we always take ratios of spectra at different angles and measure the absolute intensity in forward direction using the photodiode to obtain a reference point for absolute photon number and luminance as discussed below.

The calibration spectrum is specific to each spectrometer and fiber and thus the combination of spectrometer and fiber used must be carefully calibrated as specified by the manufacturer of the spectrometer prior to taking any data. The calibration generally involves measuring the dark counts from the spectrometer and the spectrum of a calibration lamp with known emission spectrum to correct for the response of the spectrometer and the fiber at different wavelengths. However, again it is not necessary to obtain an absolute calibration. It is instead sufficient to ensure that the relative calibration between different wavelengths is accurate.

4. Theory

The theoretical description given in the following is based on and derived from the literature^[38–40] and explained in more detail in Section 2 of the Supporting Information.

The EQE is defined as

$$\eta_{\text{EQE}} = \frac{N_{\text{ph}}}{N_e} \quad (2)$$

where N_{ph} is the total number of photons per second leaving the device and $N_e = I_{\text{OLED}}(V) q^{-1}$ is the number of electrons per second injected into the device, with $I_{\text{OLED}}(V)$ denoting the OLED current at voltage V and q the elementary charge. N_{ph} can be obtained from the number of photons emitted in forward direction and the relative photon number at each angle, expressed through a correction factor $F_E(\theta)$

$$N_{\text{ph}} = \frac{I_0(V)}{\bar{E}_{\text{ph}}} 2\pi \int_0^{\frac{\pi}{2}} F_E(\theta) \sin \theta d\theta \quad (3)$$

where I_0 is the radiant intensity and \bar{E}_{ph} is the average photon energy of light emitted by the OLED in forward direction. For a Lambertian emitter, by definition, $F_E(\theta) = \cos \theta$. However, the majority of OLEDs do not follow perfect Lambertian emission characteristics, with some designs deviating substantially from ideal Lambertian. We thus explicitly calculate $F_E(\theta)$ from the experimentally determined spectral radiant intensity $S(\lambda, \theta)$ as

$$F_E(\theta) = \frac{\int S(\lambda, \theta) \lambda d\lambda}{\int S(\lambda, 0) \lambda d\lambda} \quad (4)$$

We can find I_0 from the measured photodiode voltage V_{PD}

$$I_0 = \frac{r^2 V_{\text{PD}}}{A_{\text{PD}} R_{\text{PD}}} \frac{\int S(\lambda, 0) d\lambda}{\int S(\lambda, 0) R(\lambda) d\lambda} \quad (5)$$

where r is the distance between the OLED and the photodiode, and A_{PD} , R_{PD} , and $R(\lambda)$ are the effective area, the resistance and the spectral responsivity of the photodiode, respectively (see Section 1.2 in the Supporting Information). The average photon energy \bar{E}_{ph} in forward direction is given by

$$\bar{E}_{\text{ph}} = hc \frac{\int S(\lambda, 0) d\lambda}{\int S(\lambda, 0) \lambda d\lambda} \quad (6)$$

Combining the above leads to the following expression for the EQE (in %)

$$\eta_{\text{EQE}}(V) = 100 \frac{2\pi r^2 V_{\text{PD}}(V)}{hc A_{\text{PD}} R_{\text{PD}}} \frac{q}{I_{\text{OLED}}(V)} \times \frac{\int S(\lambda, 0) \lambda d\lambda}{\int S(\lambda, 0) R(\lambda) d\lambda} \int_0^{\frac{\pi}{2}} F_E(\theta) \sin \theta d\theta \quad (7)$$

Unlike the EQE, the luminous efficacy η_p is a photometric quantity. It has units of lm W^{-1} and is given by the ratio of the emitted luminous flux Φ_v to the consumed electrical power VI_{OLED}

$$\eta_p = \frac{\Phi_v}{V I_{\text{OLED}}} \quad (8)$$

In order to obtain any photometric quantity X_v from its radiometric counterpart X_E , one has to convolve with the normalized sensitivity function of the human eye $v(\lambda)$ and scale with the photopic constant K_m

$$X_v = K_m \int X_E v(\lambda) d\lambda \quad (9)$$

Using this and the derivation of Φ_v in Section 2.2 of the Supporting Information, leads to

$$\eta_p(V) = 2\pi \frac{r^2 V_{\text{PD}}(V)}{A_{\text{PD}} R_{\text{PD}}} \frac{K_m}{V I_{\text{OLED}}(V)} \times \frac{\int S(\lambda, 0) v(\lambda) d\lambda}{\int S(\lambda, 0) R(\lambda) d\lambda} \int_0^{\frac{\pi}{2}} F_v(\theta) \sin \theta d\theta \quad (10)$$

where the relative photopic response at each angle is given by

$$F_v(\theta) = \frac{\int S(\lambda, \theta) v(\lambda) d\lambda}{\int S(\lambda, 0) v(\lambda) d\lambda} \quad (11)$$

5. Exemplary Analysis

In the following, we discuss exemplary measurement results taken with our measurement setup for three different OLEDs. Device 1 (Figure 4a) is a blue, bottom-emitting device with an

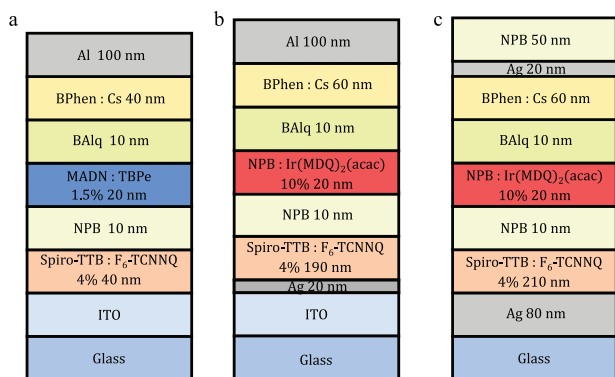


Figure 4. Stack architecture of the three different OLEDs used to illustrate device characterization with our measurement system. a) Bottom-emitting fluorescent blue OLED (Device 1). b) Bottom-emitting phosphorescent red OLED (Device 2). c) Top-emitting phosphorescent red microcavity OLED (Device 3). Doping concentrations given are in wt%.

active area of 16 mm². Device 2 (Figure 4b) is a red, bottom-emitting device, with an active area of 4 mm². Device 3 (Figure 4c) is a red, top-emitting microcavity OLED also with an active area of 4 mm².

As explained in Section 3.5, in practice it is usually most convenient to record the IVL characteristics first and then record angle-resolved spectra. However, for the sake of our discussion, it is easier to begin by considering the spectral characteristics. Figure 5a–c shows a false color representation of the spectral data for the three OLEDs discussed here across all measured angles, i.e., –90...90°, and for the relevant wavelength range of each OLED. The spectra have been corrected as described in Section 3.5 to provide the relative spectral radiant intensity (here normalized to the maximum). The OLEDs show an angular dispersion due to the used materials and their

geometry as can also be seen in Figure 5d–f. As expected, the emission from Devices 1 and 2 covers a relatively broad spectral and angular range, when compared to the microcavity-based Device 3. Device 3 shows a blueshift in the peak emission wavelength with increasing emission angle, which is commonly observed for a microcavity device architecture. In addition, for Device 1, the emission spectrum clearly shows the vibronic substructure of the fluorescent blue emitter material used in this OLED; the intensity of the emission also exhibits a clear angular dependency. This demonstrates again the importance of recording the complete angular variation of the spectrum to characterize OLEDs accurately.

The difference in the spectral shape of the three OLEDs becomes more apparent when directly comparing the spectra recorded in forward direction ($\theta = 0^\circ$, Figure 6a). Figure 6b shows the spectrally integrated emission intensity as a function of emission angle. The angular distribution of the emission from the microcavity OLED (Device 3) is substantially narrower than the emission from the other two devices. The emission from the blue OLED (Device 1) is super-Lambertian (i.e., higher intensity than an ideal Lambertian emitter when normalized to the emission in forward direction). By contrast, the emission from the red OLED (Device 2) is sub-Lambertian (i.e., lower intensity than Lambertian when normalized in forward direction). As discussed below, this difference leads to significant corrections to the device efficiency that one would estimate when assuming Lambertian emission.

To record the IVL characteristics of our devices, the voltage applied to the devices was scanned from –2.0 to 2.0 V in 0.5 V steps and then from 2.0 to 4.0 V in 0.1 V steps. Figure 6c shows the current density, i.e., the current recorded by the sourceme-ter divided by the active area of the device, as a function of voltage for each OLED. (Current density is calculated automatically by our software if the user provides the active area of the

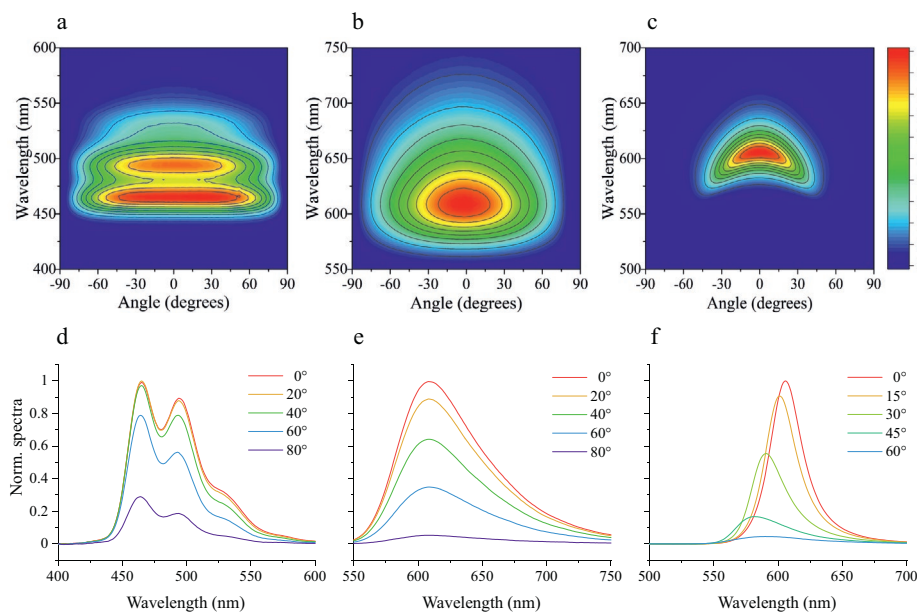


Figure 5. Measured device emission intensity across all angles and wavelengths for a) Device 1, b) Device 2, and c) Device 3. Emission spectra at varying angles normalized to peak in forward direction for d) Device 1, e) Device 2 and f) Device 3. Spectra were recorded in constant-current driving mode, at a current of 1.0 mA, and using a spectrometer integration time of 300 ms.

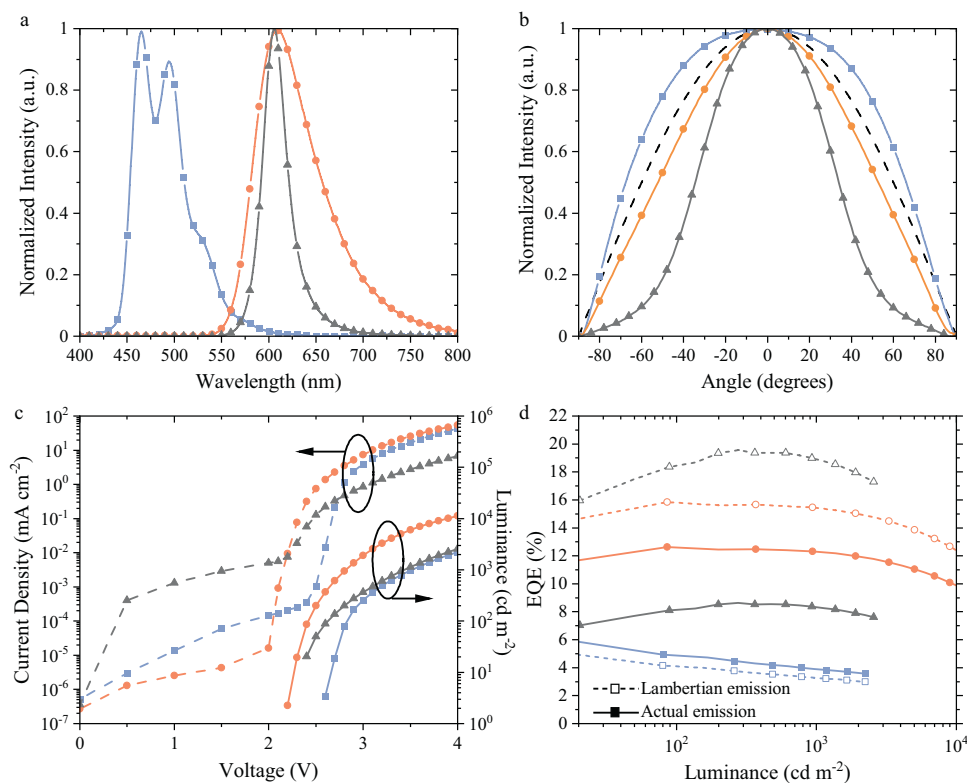


Figure 6. Representative characterization of Device 1 (blue squares), Device 2 (red circles), and Device 3 (grey triangles). a) Electroluminescence spectra in forward direction, each normalized to the maximum. b) Spectrally integrated radiant intensity as a function of the angle, normalized to the intensity in forward direction. Dashed line indicates Lambertian emission. c) IVL characteristics with dashed lines showing current density and solid lines showing forward luminance. d) EQE versus forward luminance with solid lines showing EQE after correcting for non-Lambertian emission and dashed lines showing EQE under Lambertian assumption.

device.) The plot also shows the forward luminance versus voltage. Here, the luminance is computed from the photodiode voltage as described in Section 2 in the Supporting Information. Note that determination of the luminance only requires knowledge of the photodiode voltage and the electroluminescence spectrum in forward direction; it does not depend on the angular emission characteristics. The same applies for the current efficiency (Section 2.3, Supporting Information).

From the angle-resolved data, we can then calculate the EQE and luminous efficacy. Using the example of EQE, Figure 6d compares the OLED efficiency obtained assuming Lambertian emission to the values obtained with the corrections from the angle-resolved spectra. The EQE at 1000 cd m^{-2} of forward luminance for Device 1 was 3.2% assuming Lambertian emission but 3.9%, i.e., over 1.2-fold higher, when accounting for the super-Lambertian emission. For Device 2, the EQE at 1000 cd m^{-2} was 15.4% assuming Lambertian emission but reduces to 12.2%, i.e., to less than 0.8-fold of the original value, once the sub-Lambertian emission characteristics of this device are considered. For both OLEDs, one would expect that the emission profile can be optimized to match the Lambertian characteristics more closely if the thickness of the charge transport layers, in particular the ETL, is optimized. For Device 3, the EQE was 18.9% when assuming Lambertian emission but this reduces by more than half, to 8.3% when correcting for the actual, highly sub-Lambertian emission characteristics, illustrating that, as

expected, for microcavity OLEDs it is crucial to account for the emission characteristics when determining EQE.

6. Modifications and Further Applications

This section describes three optional modifications of our measurement system, which extend its function to (1) providing an approximate measurement of the IQE of OLEDs, (2) recording angular emission characteristics of the photoluminescence from thin films, which can be used to derive the mean orientation of the emissive transition dipole moment, and (3) rapidly recording IVL characteristics from multiple OLEDs on a common substrate using an experimental setup that ensures highly reproducible positioning of samples.

6.1. Estimate of IQE: Substrate Mode Measurement

To estimate the IQE, one needs to obtain an estimate of the total amount of light generated within the OLED, including the fraction that normally remains trapped within the glass substrate due to total internal reflection. For relatively small OLED pixels, this can be achieved by optically coupling to the emissive surface of the OLED a semi-cylindrical glass lens with a radius substantially larger than the size of the OLED pixel.

Our setup uses a custom semi-cylindrical lens made from BK-7 glass as cylindrical lenses of sufficient size are not a list item with most optics providers. The lens is placed on top of a lens holder made in-house (see parts list and CAD drawings of holder in Supplementary Information, Section 1). A drop of immersion oil is put on the front of the OLED and the OLED is then pressed onto the flat surface of the lens to ensure index matching. Care should be taken that the immersion oil covers the entire interface between sample and lens and that there are no air bubbles. The device characterization is then repeated following the procedure described in Section 3. The radiant and luminous flux obtained in this way represent the total amount of light that is coupled to the OLED substrate but do not include any light that is trapped within the device stack itself, either in waveguided or plasmon modes. As such, the measured IQE generally underestimates the true IQE of the device. Optical modelling can help to determine the fraction of light trapped within the device stack and thus the true IQE of an OLED.

6.2. Photoluminescence Measurement and Dipole Orientation

The semi-cylindrical glass lens extension can also be used to record angle-resolved and polarized photoluminescence spectra of thin fluorescent films. These spectra can be used to estimate the average orientation of the transition dipole of the emissive molecules within the EML by following the procedure described in the literature.^[22,30,40–42] For this measurement, a 40 nm film of the same composition as the EML to be investigated is deposited on a glass or quartz substrate. Prior to the measurement, the film should be encapsulated by a cavity glass to prevent photo-oxidation or oxygen-induced quenching of photoluminescence.

The measurement system is extended by a UV excitation light source. Here, we use an LED with a peak emission wavelength of 365 nm. The LED was mounted at a fixed angle to the sample (e.g., 30° to the normal), using the same rail as the xyz-stage and the OLED (Figure 7). The light from the UV LED is conditioned

by a dielectric short-pass filter to block any residual emission more than 10 nm above the 365 nm emission peak of the LED. In addition, a dielectric long-pass filter (cut on wavelength, 425 nm) is placed in front of the spectrometer fiber to avoid any bleed-through of the UV excitation light. Finally, a polarizer on a rotation mount is placed in front of the spectrometer fiber to allow to distinguish photoluminescence with transverse magnetic and transverse electric polarization as required to enhance the accuracy of measurements of transition dipole orientation.

In general, the choice of UV excitation light source will depend on the excitation spectrum of the EML to be studied. A 365 nm LED is useful in many cases because this wavelength is short enough to generate photoluminescence in most EML materials, yet long enough to still penetrate a conventional encapsulation glass. In addition, 365 nm LEDs with high power are available at moderate cost. The selection of the most suitable long-pass and short-pass filters then depends on the LED wavelength and EML emission spectrum.

For the measurement, the semi-cylindrical glass lens is optically coupled to the substrate with immersion oil to extract all light from the glass substrate and thus collect as much information about dipole orientation as possible. The sample can be fixed to the semi-cylindrical lens either with a sample holder or with tape, provided that in either case there is sufficient pressure to the substrate to ensure optical contact between sample and lens. The sample is then illuminated by the UV light source through an aperture in the tape or sample holder. For consistent results, the sample needs to be illuminated evenly across the entire aperture. An aperture size of $5 \times 5 \text{ mm}^2$ provides a good compromise between generating strong photoluminescence and providing homogeneous illumination when using a close by LED light source for excitation.^[43]

Similar to the procedure for recording angle-resolved emission spectra from OLEDs, a scan across all angles is performed while the UV light source excites the sample. For the LED and LED driver listed in the parts list, the LED driver can be readily controlled from the computer via the sourcemeter. Alternatively,

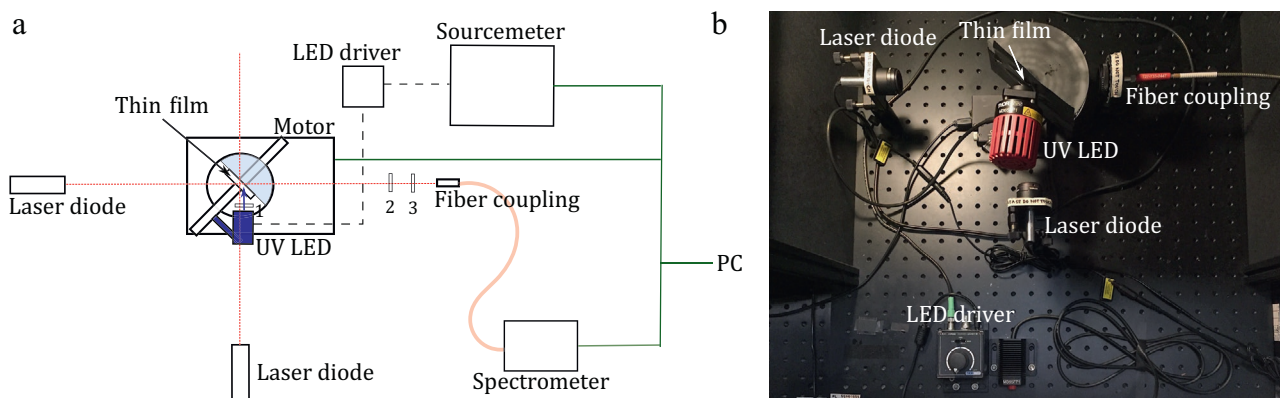


Figure 7. a) Schematic illustration of a modified goniometer setup for measuring angle-resolved photoluminescence. The OLED sample is replaced by a thin film sample on a glass substrate. A cylindrical lens (light blue semi-circle) is index-matched to the front of the glass substrate. A UV LED is mounted on the rotation stage to illuminate the sample at roughly a 30° angle and thus excite photoluminescence. A short-pass filter 1) is mounted in front of the UV LED. A long-pass filter 2) and a polarizer 3) are mounted in front of the fiber coupled to the spectrometer to reject excitation light and allow selection of photoluminescence with a specific polarization. Compare with Figure 2 for a description of the other components of the setup. b) Photograph of the actual setup.

the driver can be controlled by manually setting the drive current on the driver itself. Controlling the LED with the sourcemeter means that it can be turned off between recording spectra at different angles and thus does not illuminate the sample continuously for the entire duration of the measurement. This is only of relevance for samples that degrade very quickly and where a short exposure time is thus preferred.

6.3. Tube for Automated Measurement of Multiple Pixels

It is often desirable to test different OLED pixels that are situated on the same substrate. In most cases, the different pixels are nominally identical and are measured to test pixel-to-pixel variability in device performance. Such variability mostly originates from electrical differences and point defects, and the angle-resolved spectra are usually comparable for all pixels on the same substrate. In many cases, one can thus perform the time-consuming angle-resolved emission measurement only for one of the OLED pixels on the substrate and perform relatively quick IVL scans for the remaining pixels. A measurement setup for such quick IVL scans on multiple pixels is described in the Supplementary Information, Section 1.2. Data recorded from quick IVL scans is then combined with the angle-resolved spectral data as described in Section 5 to determine the luminance, EQE and luminous efficacy for all pixels on one substrate.

7. Conclusion

We described a system and measurement procedure to accurately measure the EQE and other key efficiency metrics of OLEDs and other thin-film LEDs. We have shown that EQE measurements can be significantly inaccurate when only recording the forward luminance and assuming Lambertian emission. For top-emitting microcavity OLEDs where the angular emission characteristics differ significantly from the ideal Lambertian profile, this simplification can lead to a >50% error in the EQE estimate, and even for conventional, bottom-emitting OLEDs, the Lambertian assumption can readily cause relative errors on the order of 20%. Our goniometer-based characterization system represents an alternative to the integrating sphere measurement and provides angular characteristics of device emission alongside an accurate EQE value. We have also presented modifications to our system that allow to estimate IQE, provide the data to determine transition dipole orientation and facilitate rapid and automated IVL measurements of multiple OLED pixels on the same substrate. With the parts list and software provided, the system can be easily replicated and adapted by other research groups.

8. Experimental Section

The OLEDs characterized in Section 5 were fabricated on either prepatterned ITO substrates with a thickness of ≈ 90 nm or neat glass substrates (1.1 mm) which were cleaned in ultrasonic baths with acetone and isopropanol. The substrates were dried with nitrogen, followed by ultraviolet ozone plasma treatment (3 min), and then placed into an evaporator chamber for high-vacuum thermal evaporation (at a

base pressure of $\approx 10^{-7}$ mbar). Evaporation rates and thicknesses were monitored by a quartz crystal balance and different shadow masks were used for the deposition of the organic layers and the metal electrode to define the structure and geometry of the active area. All organic materials were purchased from Lumtec and used without further purification. After thermal evaporation, devices were transferred from the vacuum chamber into a nitrogen-filled glovebox without intermittent exposure to air and then encapsulated with getter-embedded cavity glass lids attached by a UV-curable epoxy glue.

Supporting Information

Supporting Information is available from the Wiley Online Library or from the author. The software and CAD drawings required to reproduce the system described here can be accessed at <https://doi.org/10.17630/022e4feb-029c-4082-9518-a9da1ae3a937>. The software can also be accessed via GitHub at <https://github.com/GatherLab/Goniometer>.

Acknowledgements

E.A., S.H., and C.K. contributed equally to this work. This research was financially supported by the EPSRC NSF-CBET lead agency agreement (Nos. EP/R010595/1 and 1706207), the Leverhulme Trust (No. RPG-2017-231), the Volkswagen Foundation (No. 93404), and the Alexander von Humboldt Stiftung (Humboldt-Professorship to M.C.G.). C.K. acknowledges support from the Basic Science Research Program through the National Research Foundation of Korea (NRF) funded by the Ministry of Education (No. 2017R1A6A3A03012331). Diese Arbeit wurde mitfinanziert durch Steuermittel auf der Grundlage des vom Sächsischen Landtag beschlossenen Haushaltes.

Conflict of Interest

The authors declare no conflict of interest.

Keywords

angle-resolved electroluminescence, external quantum efficiency, goniometer, non-Lambertian emission, OLEDs, thin-film LEDs

Received: May 21, 2020
Revised: September 29, 2020
Published online:

- [1] C. W. Tang, S. A. VanSlyke, *Appl. Phys. Lett.* **1987**, *51*, 913.
- [2] R. H. Friend, R. W. Gymer, A. B. Holmes, J. H. Burroughes, R. N. Marks, C. Taliani, D. D. C. Bradley, D. A. D. Santos, J. L. Brédas, M. Lögdlund, W. R. Salaneck, *Nature* **1999**, *397*, 121.
- [3] A. J. Heeger, *Solid State Commun.* **1998**, *107*, 673.
- [4] C. D. Müller, A. Falcou, N. Reckefuss, M. Rojahn, V. Wiederhirn, P. Rudati, H. Frohne, O. Nuyken, H. Becker, K. Meerholz, *Nature* **2003**, *421*, 829.
- [5] S. R. Forrest, *Nature* **2004**, *428*, 911.
- [6] B. W. D'Andrade, S. R. Forrest, *Adv. Mater.* **2004**, *16*, 1585.
- [7] M. C. Gather, A. Köhnen, A. Falcou, H. Becker, K. Meerholz, *Adv. Funct. Mater.* **2007**, *17*, 191.
- [8] A. Sugimoto, H. Ochi, S. Fujimura, A. Yoshida, T. Miyadera, M. Tsuchida, *IEEE J. Sel. Top. Quantum Electron.* **2004**, *10*, 107.

- [9] S. Garner, D. Chowdhury, S. Lewis, *Information Display* **2019**, 35, 9.
- [10] D. Wang, J. Hauptmann, C. May, *MRS Advances* **2019**, 4, 1367.
- [11] S. K. Attili, A. Lesar, A. McNeill, M. Camacho-Lopez, H. Moseley, S. Ibbotson, I. D. W. Samuel, J. Ferguson, *Br. J. Dermatol.* **2009**, 161, 170.
- [12] A. K. Bansal, S. Hou, O. Kulyk, E. M. Bowman, I. D. W. Samuel, *Adv. Mater.* **2015**, 27, 7638.
- [13] A. Steude, E. C. Witts, G. B. Miles, M. C. Gather, *Sci. Adv.* **2016**, 2, e1600061.
- [14] A. Morton, C. Murawski, S. R. Pulver, M. C. Gather, *Sci. Rep.* **2016**, 6, 31117.
- [15] A. Morton, C. Murawski, Y. Deng, C. Keum, G. B. Miles, J. A. Tello, M. C. Gather, *Adv. Biosyst.* **2019**, 3, 1800290.
- [16] K. Yoshida, P. P. Manousiadis, R. Bian, Z. Chen, C. Murawski, M. C. Gather, H. Haas, G. A. Turnbull, I. D. W. Samuel, *Nat. Commun.* **2020**, 11, 1171.
- [17] K. Lin, J. Xing, L. N. Quan, F. P. G. de Arquer, X. Gong, J. Lu, L. Xie, W. Zhao, D. Zhang, C. Yan, W. Li, X. Liu, Y. Lu, J. Kirman, E. H. Sargent, Q. Xiong, Z. Wei, *Nature* **2018**, 562, 245.
- [18] Y. Yang, Y. Zheng, W. Cao, A. Titov, J. Hyvonen, J. R. Manders, J. Xue, P. H. Holloway, L. Qian, *Nat. Photonics* **2015**, 9, 259.
- [19] Y. Cao, N. Wang, H. Tian, J. Guo, Y. Wei, H. Chen, Y. Miao, W. Zou, K. Pan, Y. He, H. Cao, Y. Ke, M. Xu, Y. Wang, M. Yang, K. Du, Z. Fu, D. Kong, D. Dai, Y. Jin, G. Li, H. Li, Q. Peng, J. Wang, W. Huang, *Nature* **2018**, 562, 249.
- [20] B. Zhao, S. Bai, V. Kim, R. Lamboll, R. Shivanna, F. Auras, J. M. Richter, L. Yang, L. Dai, M. Alsari, X.-J. She, L. Liang, J. Zhang, S. Lilliu, P. Gao, H. J. Snaith, J. Wang, N. C. Greenham, R. H. Friend, D. Di, *Nat. Photonics* **2018**, 12, 783.
- [21] M. Anaya, B. P. Rand, R. J. Holmes, D. Credgington, H. J. Bolink, R. H. Friend, J. Wang, N. C. Greenham, S. D. Stranks, *Nat. Photonics* **2019**, 13, 818.
- [22] J. Frischeisen, D. Yokoyama, C. Adachi, W. Brütting, *Appl. Phys. Lett.* **2010**, 96, 073302.
- [23] T. D. Schmidt, T. Lampe, D. Sylvinson M.R., P. I. Djurovich, M. E. Thompson, W. Brütting, *Phys. Rev. Appl.* **2017**, 8, 037001.
- [24] K.-H. Kim, J.-J. Kim, *Adv. Mater.* **2018**, 30, 1705600.
- [25] C. Adachi, M. A. Baldo, M. E. Thompson, S. R. Forrest, *J. Appl. Phys.* **2001**, 90, 5048.
- [26] H. Uoyama, K. Goushi, K. Shizu, H. Nomura, C. Adachi, *Nature* **2012**, 492, 234.
- [27] N. C. Greenham, R. H. Friend, D. D. C. Bradley, *Adv. Mater.* **1994**, 6, 491.
- [28] A. Salehi, X. Fu, D. Shin, F. So, *Adv. Funct. Mater.* **2019**, 29, 1808803.
- [29] J. Song, K.-H. Kim, E. Kim, C.-K. Moon, Y.-H. Kim, J.-J. Kim, S. Yoo, *Nat. Commun.* **2018**, 9, 3207.
- [30] M. Flämmich, J. Frischeisen, D. S. Setz, D. Michaelis, B. C. Krummacker, T. D. Schmidt, W. Brütting, N. Danz, *Org. Electron.* **2011**, 12, 1663.
- [31] S. Möller, S. R. Forrest, *J. Appl. Phys.* **2002**, 91, 3324.
- [32] B. J. Matterson, J. M. Lupton, A. F. Safonov, M. G. Salt, W. L. Barnes, I. D. W. Samuel, *Adv. Mater.* **2001**, 13, 123.
- [33] Y.-J. Chen, W.-K. Lee, Y.-T. Chen, C.-Y. Lin, S.-W. Wen, M. Jiao, G.-D. Su, H. Y. Lin, R. J. Visser, B. L. Kwak, C.-C. Chen, W.-Y. Lin, S. Wang, C.-P. Chang, C.-C. Wu, *Adv. Sci.* **2018**, 5, 1800467.
- [34] M. C. Gather, S. Reineke, *J. Photon. Energy* **2015**, 5, 057607.
- [35] S.-Y. Kim, W.-I. Jeong, C. Mayr, Y.-S. Park, K.-H. Kim, J.-H. Lee, C.-K. Moon, W. Brütting, J.-J. Kim, *Adv. Funct. Mater.* **2013**, 23, 3896.
- [36] I. Tanaka, S. Tokito, *Jpn. J. Appl. Phys.* **2004**, 43, 7733.
- [37] G. Leschhorn, R. Young, *Handbook of LED and SSL Metrology*, Pro Business GmbH, Berlin **2017**.
- [38] S. R. Forrest, D. D. C. Bradley, M. E. Thompson, *Adv. Mater.* **2003**, 15, 1043.
- [39] (Eds. W. Brütting, C. Adachi, R. J. D. Holmes), *Physics of Organic Semiconductors*, Wiley-VCH, Weinheim, Germany **2012**.
- [40] M. Furno, R. Meerheim, S. Hofmann, B. Lüssem, K. Leo, *Phys. Rev. B* **2012**, 85, 115205.
- [41] P. Liehm, C. Murawski, M. Furno, B. Lüssem, K. Leo, M. C. Gather, *Appl. Phys. Lett.* **2012**, 101, 253304.
- [42] A. Graf, P. Liehm, C. Murawski, S. Hofmann, K. Leo, M. C. Gather, *J. Mater. Chem. C* **2014**, 2, 10298.
- [43] C. Hänisch, S. Reineke, S. Lenk, in *Organic Electronics and Photonics: Fundamentals and Devices*, (Eds: S. Reineke, K. Vandewal), SPIE, Strasbourg, France **2018**, p. 29.